Yield Strength of Glued Langmuir-Blodgett Films Determined by Friction Force Microscopy

Supporting Information

Kyle C. Wagner, Yao Wang, Steven L. Regen, and Dmitri V. Vezenov

Department of Chemistry, Lehigh University, Bethlehem, PA 18015

Set Point Ramping Code. The following function was executed from the command line to increase the set point by a defined amount over each scan line of the image:

td_WriteString("OutWave0StatusCallback","MainSetVarFunc(\"SetpointSetVar_0\",

GV(\"DeflectionSetpointVolts\")+.1,\"\",\":Variables:MasterVariablesWave[%DeflectionSetpointVolts]\")")

The code was provided by Jason Bemis of Asylum Research, Santa Barbara, CA. The program runs within the Igor 6.03A (and newer) programming interface of MFP-3D controller interface. The portion of the code "**+.1**" defines set point increment (in Volts, 0.1 V here) for each scan line of the image and may be changed by the user to produce the desired final load.

Surface Roughness. The surface roughness was measured by AFM on an area of each sample free of abnormal debris or damage. The root mean square (RMS) roughness was determined through the MFP-3D software for a 5 μm scan. Consistent with previous studies,[1] friction force is independent on the roughness of the sample (Table S1).

Table S1. Roughness values (5 µm ×5 µm) for LB films measured by AFM.

Sample	RMS Roughness (nm)
1	2.4
2	1.7
3	1.7
4	2.4
5	2.8

Measurement of the Tip Radius. The tip radius was measured by imaging an ultra-sharp silicon grating calibration standard TGT01 manufactured by MicroMasch, Tallin, Estonia. Veeco NP series probes have an overall pyramidal shape, with apex often asymmetrical in shape, thus we determined the effective tip radius according to: $2/R_{eff} = 1/R_1 + 1/R_2$. Figure S1 shows a typical image of the silicon nitride tip formed by a sharp feature of the silicon grating along with the line profiles in the vertical and horizontal directions.

(a)

(b)
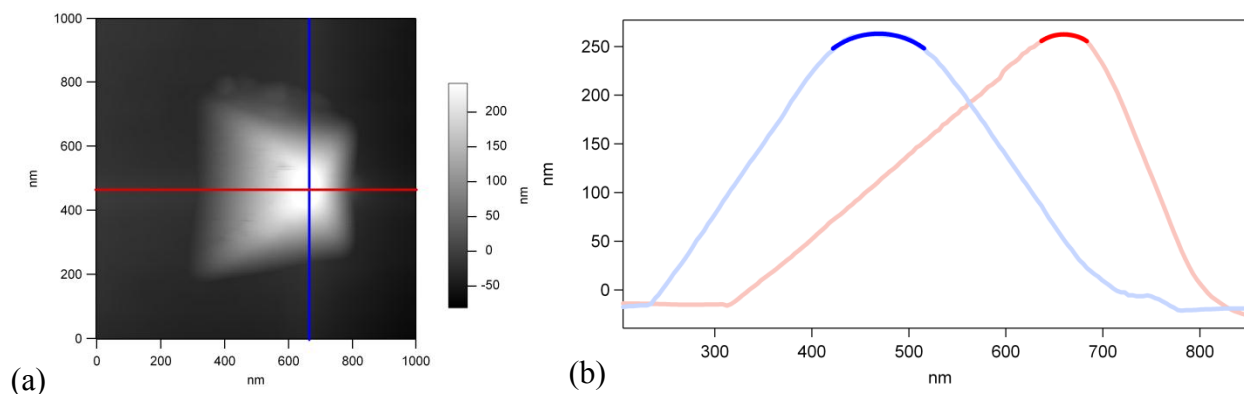
Figure S1. a) Height image of an ultra-sharp spike on a TGT01 calibration grating, b) Line profiles of the tip image fitted with a sphere equation (dark lines) at the apex of the peak.

The height image of the tip was examined using line profiles going trough the apex of the tip in two orthogonal directions. The top section of each profile $h(x)$ was fitted with an equation for a sphere $h(x) = h_0 + \sqrt{R^2 - (x - x_0)^2}$ to find the radii R_x and R_y. The reported values of tip radii were measured on several different ultra-sharp silicon features (3-4) and the average tip radius was 130 nm.

Determination of the Tabor Parameter. The Tabor parameter,[2] μ_T, is used to quantify the transition between the DMT[3] and JKR[4] regimes for surface deformations and defined by:

$$\mu_T = \left(\frac{16 R W^2}{9 K^2 z_0^3} \right)^{1/3} \tag{S1}$$

where z_0 is the equilibrium separation of the surfaces (typically ~0.1 nm), R is the radius of the probe (130 nm), K is the elastic modulus of the tip-sample interface (18.9 GPa), and W is the work of adhesion (between $1.5 L_C/(\pi R)$ and $2 L_C/(\pi R)$ or 63-84 mJ/m^2 depending on the selected contact mechanics model, using an adhesion force of 51.3 nN from the force-distance curves on octadecyltrichlorosilane (OTS) self-assembled monolayer (SAM) on silicon).[5] The Tabor parameter is calculated to be approximately $1.4 - 1.7$. This value is in an intermediate region between the DMT and JKR models, but is more characteristic of the DMT model. The transition to the JKR model occurs when $\mu_T > 3$.[2]

The Tabor parameter and the Maugis-Dugdale[6] parameter are approximately equivalent and may be replaced by a single transition parameter, α.[5] For an intermediate fitting model the value of α varies between 0 and 1: where $\alpha=0$ corresponds to the DMT model and $\alpha=1$ represents

the JKR model.[5] It is also possible to fit the experimental data with the following equation to determine the extent to which our data follows the transition between DMT and JKR contact mechanics models.

$$F(L) = F_C \left(\frac{\alpha + \sqrt{1 - \dfrac{L}{L_C}}}{1 + \alpha} \right)^{4/3} \qquad (S2)$$

where $F(L)$ is the friction force, F_C is the friction force at zero load, L is the applied load, and L_C is the adhesion force. Figure S2 shows the results of fitting the friction-load curves on clean OTS SAM with the intermediate, DMT, and JKR equations (friction data were obtained with the same AFM probe as was used in the experiments on LB films described in the main text of the paper). The intermediate fit with α=0.7 provides the best fit of our data and corresponds to μ_T of ~1, in reasonable agreement with the estimations made above.
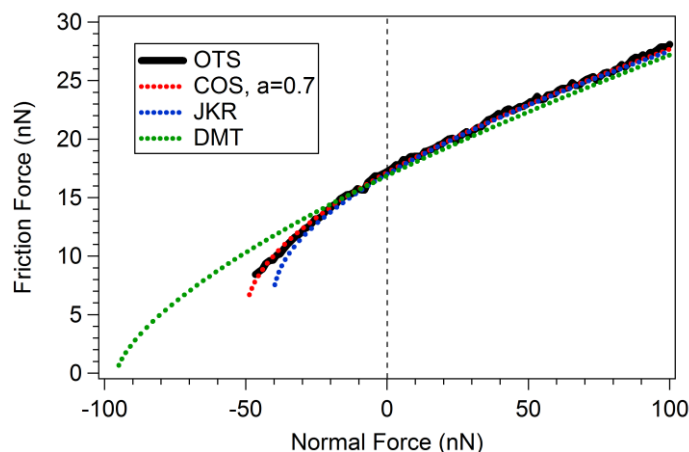
Figure S2. Fitting of an OTS friction versus load curve with equations for the COS, DMT, and JKR models. The intermediate model with α=0.7 provides the best fit to our data.

Wedge Calibration Method. The wedge calibration method is one of the commonly used methods to determine the lateral sensitivity of the detector and the procedure may be found in

several sources.[7, 8] In order to carry out the wedge calibration, we used a triangular calibration standard (TGG01, MikroMasch, Tallin, Estonia). The calibration standard was rotated at several angles (30-60 ° with respect to the long dimension of the cantilever) in order to decrease the slope of the wedge to eliminate undesired stick-slip phenomenon (observed when scanning normal with respect to the lines in the pattern) as well as to avoid contact between the wedge and the sidewalls of the tip (the tip sidewalls and the wedge have approximately the same slope). Friction versus load curves were obtained using our standard procedure: the normal set point was incremented on a line-by-line basis on a nominally single scanning location. Figure S3a shows the topography of the wedge standard rotated at 60°. Figure S3b is the height image of the surface with the scanning fixed on a single scan line and Figure S3c is a line profile of the surface. The left side is sloped at 30.7° and the right side has a slope of -42.2°.

(a)

(b)

(c)
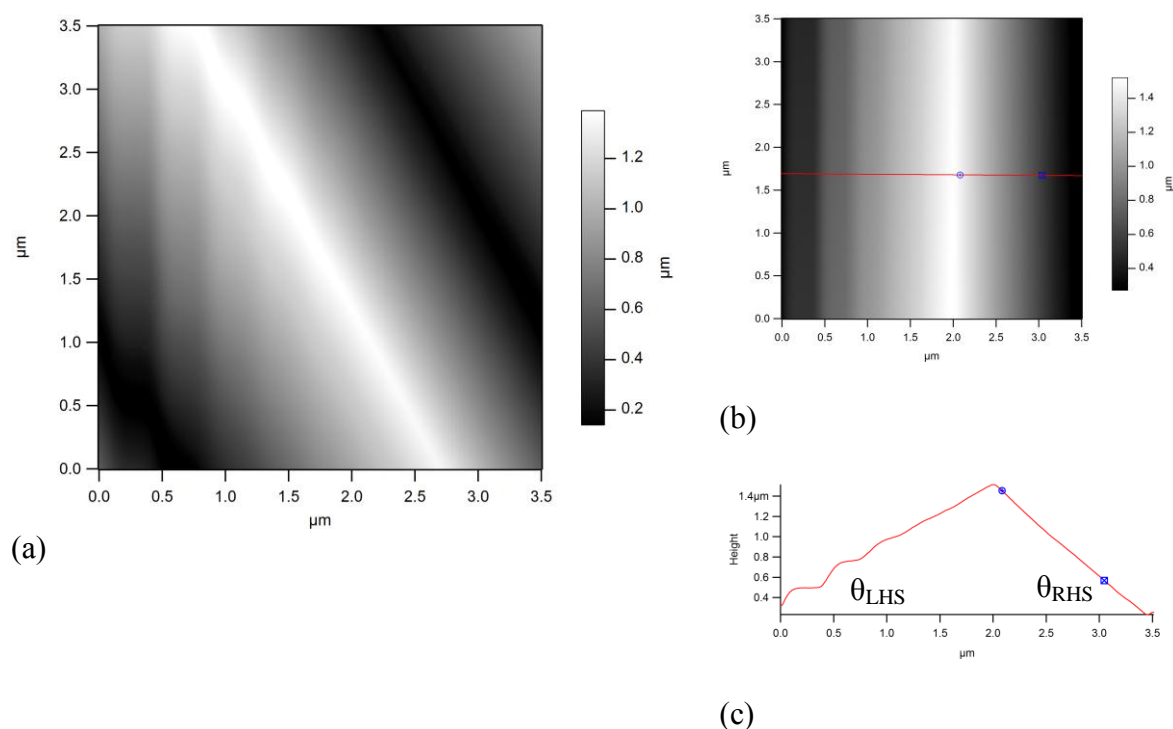
FIGURE S3. (a) Topography of the TGG01 wedge standard rotated at an angle of 60° with respect to the long axis of the cantilever; (b) Topography of (a) with scanning locked on a single scan line; (c) Line profile of (b).

5

We slopes for the two sides of the wedge were different by design, therefore, the calculation was carried out for each side using experimental slopes. For notation, we will refer to the two sides of the wedge as left-hand-side (LHS) and right-hand-side (RHS). Figure S4 is a plot of the lateral signal (Volts), $F^{(V)}$, versus normal load (Volts), $L^{(V)}$. From this plot, we can determine (Figure S5) the friction loop offset $\Delta=(Lateral_{trace}+ Lateral_{retrace})/2$, and the friction force $F=(Lateral_{trace}- Lateral_{retrace})/2$, for both LHS and RHS (*trace* and *retrace* refer to scanning in two opposite directions – left to right and right to left). From the data in Figure S5, the slopes $\Delta'=d\Delta/dL$ and $F'=dF/dL$ can be obtained and used to calculate the friction coefficient.
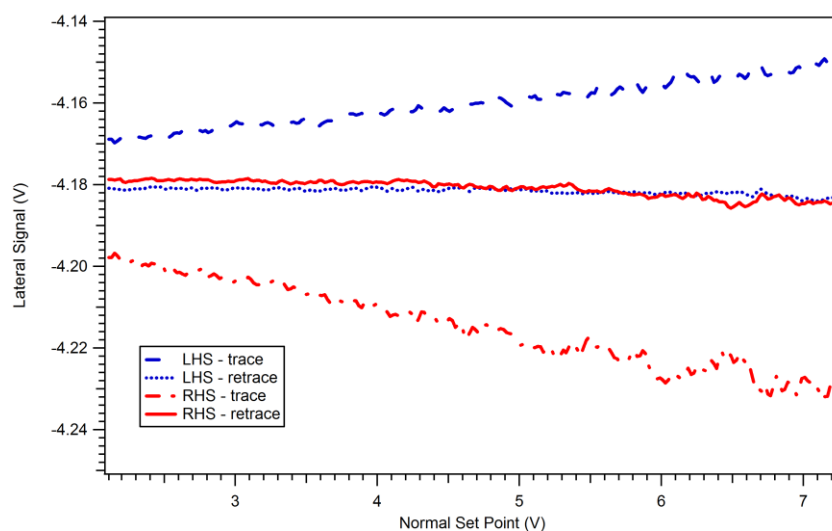
FIGURE S4. Lateral signal (Volts) versus applied load (Volts) for LHS and RHS from Figure S3b.

6
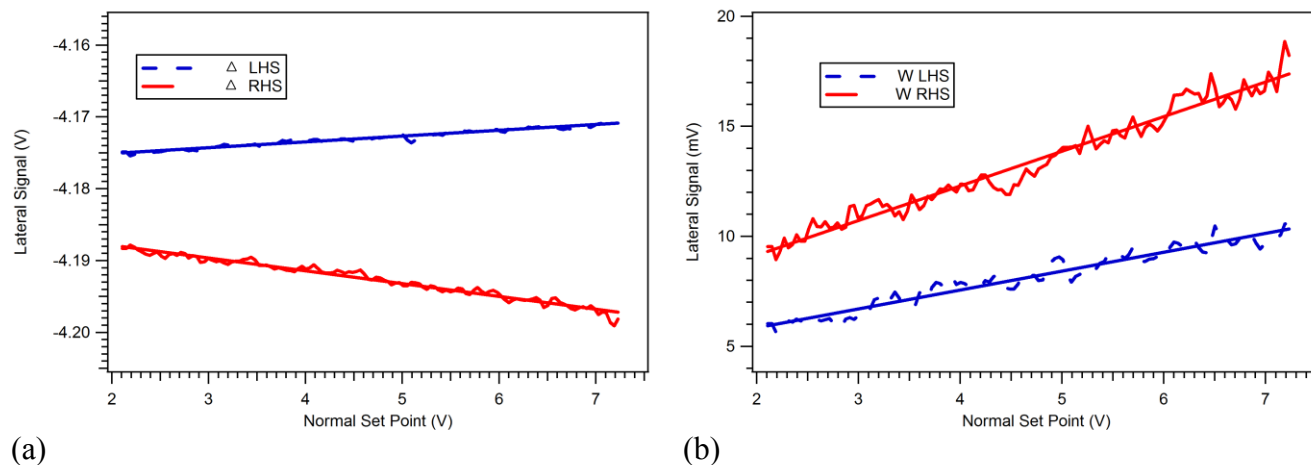
FIGURE S5. Friction loop offset Δ (a) and friction force F (b) as a function of applied normal load L for LHS and RHS.

To improve statistical treatment of the calibration data, we carried out calculation of the slopes $\Delta'=d\Delta/dL$ and $F'=dF/dL$ at multiple points in the vicinity of the ridge apex (Figure S6). The average values of the slopes Δ' and F' led to a value of friction coefficient $\mu = 0.47\pm0.07$ determined as previously described.[7]
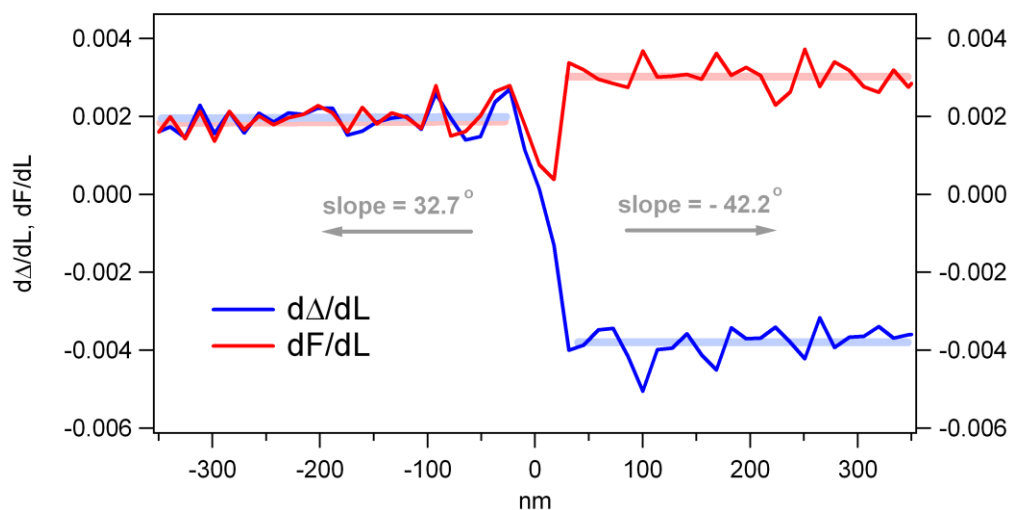
FIGURE S6. The slopes $\Delta'=d\Delta/dL$ and $F'=dF/dL$ for multiple points in the vicinity of the ridge (located at x=0 nm).

The change in friction with increase in the applied normal load is a function of μ and θ. In order to convert from $F^{(V)}$ to friction in units of force, $F^{(N)}$, a conversion factor, S_x, is introduced. A similar conversion factor, S_z, is introduced for the normal load.

$$\frac{dF^{(N)}}{dL^{(N)}} = \frac{S_x dF^{(V)}}{S_z dL^{(V)}} = \frac{\mu}{\cos^2\theta - \mu^2\sin^2\theta} \tag{S3}$$

$$S_x = \frac{\mu}{\cos^2\theta - \mu^2\sin^2\theta}\left(\frac{dF^{(V)}}{dL^{(V)}}\right)^{-1} S_z \tag{S4}$$

or, similarly:

$$S_x = \frac{\left(1+\mu^2\right)\sin\theta\cos\theta}{\cos^2\theta - \mu^2\sin^2\theta}\left(\frac{d\Delta^{(V)}}{dL^{(V)}}\right)^{-1} S_z \tag{S5}$$

The experimentally measured z-deflection sensitivity was $S_{InvOLS} = 44.2$ nm/V and the normal spring constant was $k_z = 0.411$ N/m, thus, $S_z = S_{InvOLS}\, k_z = 18.2$ nN/V. With mean values of $F'(\mu,\theta)$ and $\Delta'(\mu,\theta)$ from multiple images (similar to the results shown in Figure S6), the average value for S_x was determined to be 5.31 ± 0.62 nN/mV.

Pseudo 2-D Height Images of Film Damage. Typically, our experimental friction versus load curves displayed damage regions with some level of secondary structure. This effect is likely a result of initiation of failure at multiple point defects in the film, followed by growth/propogation of the defects along the scan line until complete removal of the film as the normal load is increased in successive scan lines. Below is an example height image of how damage usually initiates in a small area and propagates to complete film failure (Film **2**). The localized damage

8

point corresponds to the point in the friction versus load curves at the onset of damage (i.e. the terminus of stable friction behavior) where damage forces were measured for calculations.

a.)   b.)
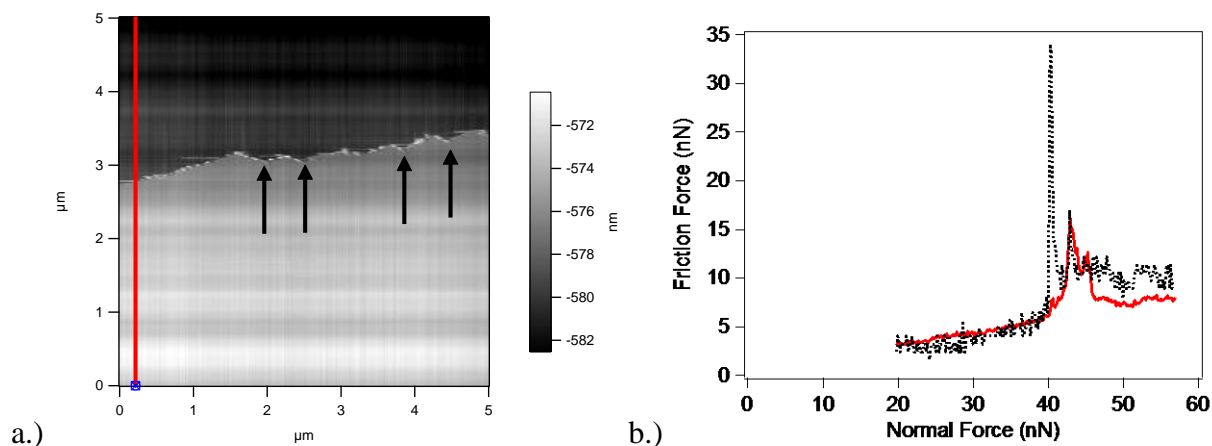
Figure S7. a.) Height image of continually increasing applied set point (set point increases from bottom of the image to the top). b.) Dotted line corresponds to calculated friction along the indicated line in the height image against the total average friction versus load curve (solid line).

Film Indentation Curves. Figure S8 displays the indentation curves for all films. Each indentation curve is the average of at least 20 individual indentation curves.
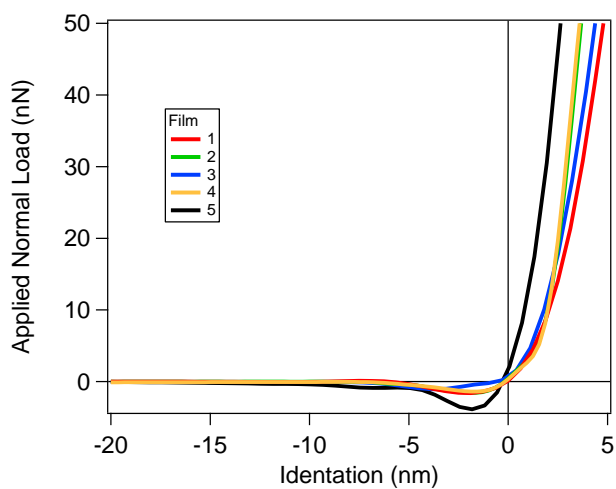
Figure S8. Averaged indentation curves for LB bilayer films.

References

1. Bhushan, B.; Kulkarni, A. V.; Koinkar, V. N.; Boehm, M.; Odoni, L.; Martelet, C.; Belin, M., *Langmuir* **1995,** *11* (8), 3189-3198.
2. Greenwood, J. A., *Proceedings of the Royal Society of London Series a-Mathematical Physical and Engineering Sciences* **1997,** *453* (1961), 1277-1297.
3. Derjaguin, B. V.; Muller, V. M.; Toporov, Y. P., *J. Colloid Interface Sci.* **1975,** *53*.
4. Johnson, K. L.; Kendall, K.; Roberts, A. D., *D. Proc. R. Soc. London A* **1971,** *324*.
5. Carpick, R. W.; Ogletree, D. F.; Salmeron, M., *Journal of Colloid and Interface Science* **1999,** *211* (2), 395-400.
6. Maugis, D., *Journal of Colloid Interface Science* **1992,** *150* (1), 243-269.
7. Ogletree, D. F.; Carpick, R. W.; Salmeron, M., *Review of Scientific Instruments* **1996,** *67* (9), 3298-3306.
8. Tocha, E.; Schonherr, H.; Vancso, G. J., *Langmuir* **2006,** *22* (5), 2340-2350.